

<https://doi.org/10.1038/s41545-024-00334-5>

# Enhanced photocatalytic performance of a rGO-Ca<sub>2</sub>Fe<sub>2</sub>O<sub>5</sub> nanocomposite for photodegradation of emergent pollutants

Check for updates

Durga Sankar Vavilapalli<sup>1</sup> ✉, Leiqiang Qin<sup>1</sup>, Justinas Palisaitis<sup>2</sup> & Johanna Rosen<sup>1</sup> ✉

In this study, a simple thermal reduction process is used to synthesize a rGO-Ca<sub>2</sub>Fe<sub>2</sub>O<sub>5</sub> (rGO-CFO) nanocomposite, with the morphological and optical characteristics of the CFO nanomaterial being modified by the rGO incorporation. The interface between rGO nanosheets and CFO nanoparticles facilitates efficient charge separation and resulting transfer of photogenerated charge carriers across the rGO nanosheets, demonstrated from photoluminescence and Mott-Schottky tests. Compared to CFO (2.1 eV), rGO-CFO has a reduced band gap energy of 1.9 eV. As synthesized nanocomposites were initially optimized and utilized for photodegradation of organic effluent Methylene blue (MB). An addition of 5 wt% rGO to the CFO demonstrated an improved photodegradation efficiency (97%) compared to bare CFO (72%). An active species trapping experiment was used to assess the MB photodegradation mechanism. The results demonstrate that hydroxyl radicals and holes are the major active species involved in photodegradation. The optimized composition (5rGO-CFO) was further tested for degradation of Bisphenol-A and Tetracycline (antibiotic). Altogether, these investigations show that the rGO-CFO is a highly efficient photocatalyst that can be used to remediate emerging contaminants in sunlight.

A healthy ecosystem is dependent on access to clean water<sup>1</sup>. The rapid expansion of industrial and agricultural activity over the past few decades has raised severe environmental concerns regarding water pollution<sup>2,3</sup>. The biotic habitat and human health are negatively impacted by toxic organic contaminants that have accumulated in water bodies, and it is quite challenging to remove these persistent pollutants<sup>4-7</sup>. For example, organic dyes (e.g. Methylene blue (MB), Methylene orange, Congo red, etc.), pesticides, phenols, pharmaceuticals, and antibiotics and their metabolites have been shown to be exceedingly harmful. Due to challenges like low biodegradability, and a protracted lifespan of deterioration in the ecosystem, the resulting contaminants after the treatment are also considered hazardous<sup>8-11</sup>.

Traditional wastewater treatment techniques, including filtration, adsorption, chemical coagulation, biological treatment, flocculation, etc., are typically ineffective at degrading aromatic and heterocyclic groups in their molecular structure. For instance, filtration (such as membrane and depth filtration) suffers from being clogged easily by foreign particles in the wastewater, and regular membrane replacement and filtration processes are

often expensive. Another efficient treatment method is adsorption, although recovering the material after the pollutant adsorption is difficult and can cause secondary contamination. The chemical coagulation process generates a large amount of sludge and is responsible for secondary pollution if the produced sludge is not handled properly. Although the biological treatment process is considered to be the most cost-effective and environmentally friendly treatment method, some complex contaminants are difficult to break down because of their bio-persistence. Consequently, there are drawbacks to the physical, chemical, and biological effluent treatment methods now being in use<sup>12,13</sup>.

The degradation and mineralization of organic pollutants into their most stable oxidation state, such as water, carbon dioxide, and the oxidized inorganic anions, or into less hazardous and easily degradable species, should be taken into consideration during remediation<sup>14-17</sup>. As a result, considerable efforts have been made globally to create appropriate, effective, and environmentally acceptable procedures for the removal of persistent pollutants. However, some strategies are overlooked for their remediation. Recent studies have concentrated on exploring the advanced oxidation

<sup>1</sup>Materials Design Division, Department of Physics, Chemistry and Biology (IFM), Linköping University, SE-581 83 Linköping, Sweden. <sup>2</sup>Thin Film Physics Division, Department of Physics, Chemistry and Biology (IFM), Linköping University, SE-581 83 Linköping, Sweden. ✉e-mail: [durga.sankar.vavilapalli@liu.se](mailto:durga.sankar.vavilapalli@liu.se); [johanna.rosen@liu.se](mailto:johanna.rosen@liu.se)

process (AOP), which makes use of semiconductor nanoparticles like metal-oxide-based semiconductors, e.g.,  $\text{TiO}_2$ ,  $\text{ZnO}$ ,  $\text{SnO}_2$ ,  $\text{MnO}_2$ ,  $\text{Fe}_2\text{O}_3$ ,  $\text{SiO}_2$ ,  $\text{Al}_2\text{O}_3$ ,  $\text{ZrO}_2$ ,  $\text{WO}_3$ ,  $\text{Cu}_2\text{O}$ , and  $\text{V}_2\text{O}_5$ , with suitable physical and chemical characteristics to support the photocatalytic AOP. Yet, the wide bandgap and the high electron-hole recombination in existing semiconductor materials limit their practical application in photocatalytic wastewater treatment<sup>13,18,19</sup>. For example, even though  $\text{TiO}_2$  is a very promising photocatalyst because of its chemical stability, non-toxicity, and low cost, the wide bandgap (3.2 eV) of  $\text{TiO}_2$  limits its optical light absorption to the UV region only, which is just 5% of the entire solar spectrum. Therefore, the photocatalytic performance in natural sunlight or visible light is not effective<sup>20</sup>. Brownmillerite  $\text{Ca}_2\text{Fe}_2\text{O}_5$  (CFO) has demonstrated excellent photocatalytic activity for the degradation of organic pollutants owing to the narrow band gap energy of 2.1 eV and reasonable visible-light harvesting<sup>20,21</sup>. The multifunctional material is also promising for energy and environmental applications, such as fuel cells, supercapacitors, batteries, and for  $\text{CO}_2$  capture, attributed mostly to its multifaceted properties like those observed in catalysis and for mixed ionic electronic conduction (MIEC)<sup>22,23</sup>. CFO with ordered oxygen vacancies and a smaller optical bandgap is anticipated to be beneficial for photocatalytic applications. Oxygen vacancies in these brownmillerites can act as photoinduced charge traps to suppress the recombination of photogenerated charge carriers. However, its application has been hampered due to the high recombination rate of photogenerated electron-hole pairs in the CFO. In our previous work, we investigated nitrogen-doped CFO and  $\text{g-C}_3\text{N}_4$ /CFO heterostructures with the aim of improving the CFO photocatalytic performance by reduction of photogenerated electron-hole recombination and by increasing light absorption<sup>20,21</sup>. The rapid separation of the excited electrons and holes in the conduction band is a key parameter that decreases the electron-hole recombination rate. This can be achieved by doping other atoms in the CFO microstructure and through the formation of CFO heterojunctions<sup>21</sup>. Furthermore, the combination of the CFO with carbonaceous materials that have a high specific surface area is also considered a pragmatic avenue for improving the photocatalytic activity of the CFO.

Two-dimensional (2D) materials with distinctive chemical and physical properties have been extensively explored in the area of photocatalysis<sup>23–28</sup>. The surface of the well-known 2D nanostructured material graphene oxide (GO) comprises oxygen functional groups, which allows it to disperse in water. Thermochemically reduced GO (rGO) has improved electron mobility, which reduces electron-hole recombination and raises the overall photocatalytic activity<sup>29</sup>. A combination of rGO and CFO may therefore provide a morphology that improves reactant diffusion. Additionally, this may facilitate that the reactant molecules reach the photocatalyst surface's active sites to boost the photocatalytic activity. Hence, the potentially advantageous characteristics of rGO-CFO nanocomposites can make them an appealing photocatalyst for industrial use, though this materials combination is unexplored. Therefore, the objective of this study is to synthesize the rGO-CFO photocatalyst by a thermal reduction method and to characterize its structural, morphological, and optical properties. Furthermore, the photocatalytic activity of the nanocomposite is studied for the degradation of emerging pollutants in the form of methylene blue (MB), Bisphenol-A (BPA), and tetracycline (TC) photodegradation under simulated sunlight.

## Methods

### Preparation of CFO

$\text{Ca}_2\text{Fe}_2\text{O}_5$  (CFO) nanoparticles were synthesized using the chemical route method<sup>30</sup>. Initially, high purity 2.04 g  $\text{Ca}(\text{NO}_3)_2 \cdot 4\text{H}_2\text{O}$  (Sigma Aldrich, 99.99%) and 2.95 g  $\text{Fe}(\text{NO}_3)_3 \cdot 9\text{H}_2\text{O}$  (Sigma Aldrich, 99.95%) were dissolved in DI water and a proportionate amount (0.83 g) of citric acid (CA) was added and stirred at room temperature. The pH of the solution was maintained at ~6–7 using Ammonia solution. The temperature of the hot plate was thereafter increased to 80 °C. Once the solution turned viscous, ethylene glycol (EG) was added to the suspension by keeping the EG/CA ratio at 1.2. Then the product was heated at 300 °C to obtain a dry mass,

which was calcined further at 700 °C for 6 h in a furnace to obtain nanostructured CFO.

### Preparation of GO

Graphene Oxide (GO) was prepared using a modified Hummer method<sup>31</sup>. 1 g of graphite flakes were added to a 9:1 mixture of concentrated  $\text{H}_2\text{SO}_4/\text{H}_3\text{PO}_4$  (90:10 mL) at 0 °C, then 6 g of  $\text{KMnO}_4$  was slowly added and stirred for one hour at 0 °C. The solution was then heated to 50 °C and stirred for 12 h. The reaction was cooled to room temperature and poured into ice water containing 5 mL of 30%  $\text{H}_2\text{O}_2$ . The solid material was then washed in succession with 200 mL of 1 M HCl and 200 mL of water. The resulting solid dispersion was dialyzed extensively to remove residual metallic ions and acids with distilled water for one week. The dialyzed solid dispersion was sonicated for two hours, then centrifuged at 8000 rpm for one hour, and finally, the solid GO was obtained by freeze-drying.

### Preparation of rGO-CFO nanocomposite

GO was initially dispersed in 10 ml of DI water and ultrasonicated for 30 min. Once the GO flakes were completely dispersed in water, 100 mg of CFO nanoparticles were dispersed in the same solution. The obtained suspension was shaken using a shaker for 30 min, and was further centrifuged to remove the water. After centrifugation, the GO-CFO samples were dried at 80 °C in a vacuum oven for 15 h. In order to obtain reduced GO-based composites (rGO-CFO), the GO-CFO samples were kept in the furnace in a  $\text{N}_2$  gas flow at 500 °C for 6 h with a heating rate of 1 °C/min. rGO-CFO samples were prepared with different wt% of rGO in the CFO; 1, 5, 10 and 15 wt%, these samples were labelled 1rGO-CFO, 5rGO-CFO, 10rGO-CFO, and 15rGO-CFO, respectively.

### Characterization

The morphology and microstructure of the synthesized samples were examined using scanning electron microscopy (SEM, Zeiss, Sigma 300) and scanning transmission electron microscopy (STEM, Linköping's double-corrected FEI Titan<sup>3</sup> 60-300) imaging. The crystallographic and phase analyses were performed using X-ray diffraction (XRD, Rigaku X-ray diffractometer, Cu K $\alpha$  source,  $2\theta = 10\text{--}80^\circ$ ). The presence of rGO in rGO-CFO composites was confirmed by using a Raman spectrometer (LabRAM HR, HORIBA). Raman spectra were recorded in the range of 100–3500  $\text{cm}^{-1}$  by using a laser excitation wavelength of 532 nm. The valence states of constituent elements were investigated through X-ray photoelectron spectroscopy (XPS, Kratos AXIS Ultra, UK). The peak fitting was carried out using CasaXPS software. The optical absorption spectra of samples were recorded using UV-visible spectroscopy (Shimadzu, UV2600i). Photoluminescence (PL) spectra were recorded using the FLS1000 (Edinburgh Instruments) with a Xenon arm lamp source excitation wavelength of 450 nm.

### Mott-Schottky tests

The Mott-Schottky tests were conducted on a standard three-electrode electrochemical system. To prepare the working electrode, 5 mg of catalyst, 250  $\mu\text{l}$  of deionized water, 250  $\mu\text{l}$  of ethanol, and 10  $\mu\text{l}$  of 5 wt% Nafion<sup>®</sup> were mixed and ultrasonicated for 30 min. Then, 5  $\mu\text{l}$  ink was drop casted on a glassy carbon electrode (diameter = 3 mm) as the working electrode, a platinum wire served as the counter electrode and Ag/AgCl as the reference electrode, evaluated at a 1 kHz frequency with 5 mV AC amplitude in 1 M  $\text{Na}_2\text{SO}_4$  solution.

### Photocatalytic experiments

The photocatalytic tests were carried out as follows: Initially, 10 ppm of methylene blue (MB), bisphenol-A (BPA), and Tetracycline (TC) aqueous solutions were prepared. 10 mg photocatalyst was dispersed into 50 ml of effluent solution. The suspended solution was magnetically stirred in the dark for 20 min to achieve an adsorption-desorption equilibrium. Then the effluent-catalyst suspension was irradiated under simulated sunlight at standard test conditions (STC) (300 W, Xe-lamp source with 100  $\text{mW}/\text{cm}^2$  (1 sun) irradiation, AM1.5). At time intervals of 10 min, effluent solution

was collected and centrifuged. The concentration of effluent was detected by measuring the maximum absorbance of effluent solutions using UV-visible absorption spectroscopy (Shimadzu, UV2600i). Liquid chromatography through quadrupole time-of-flight mass spectrometry (LC QTOF-MS, Agilent 1290 Infinity) was used to analyze the degraded by-products after and during the photocatalytic degradation of effluents.

## Results and discussion

The morphology of the CFO, rGO, and rGO-CFO samples are shown in Fig. 1a–c. The spherical CFO nanoparticles (NPs) tend to join and agglomerate owing to the magnetic dipolar interactions, and van der Waals forces<sup>32</sup>. The average particle size of CFO for all samples is around ~80 nm. The average crystallite size was found to be around 31 nm using XRD. Well-defined free-standing rGO nanoflakes, shown in Fig. 1b, are developed by reducing GO. In the rGO-CFO samples, CFO nanoparticles are homogeneously distributed on the rGO sheets. This may increase the distance between the rGO nanosheets, which improves the active surface and thus enhances the photocatalytic performance. The presence and distribution of CFO NPs on rGO nanosheets are clearly resolved in the STEM image (Fig. 1d).

Structural characteristics of the as-prepared precursors and the annealed samples were characterized by XRD analysis, as shown in Fig. 2a. All XRD peaks of the as-prepared CFO precursor and the rGO-CFO composites were well matched with the orthorhombic (*pnma*) phase  $\text{Ca}_2\text{Fe}_2\text{O}_5$ <sup>20,21</sup>. Furthermore, all diffraction peaks of the composites were well-matched with CFO, and the absence of additional peaks reveals the high purity of the synthesized material. In the rGO-CFO composite, no rGO peaks were observed, indicating the likely dispersion of the sheets of rGO because of interleaved CFO nanoparticles, as observed in the SEM and TEM analysis (Fig. 1c, d). Furthermore, the CFO and rGO-CFO were examined by Raman spectroscopy to determine the surface functional groups, shown in Fig. 2b. Raman peaks occurring at  $231\text{ cm}^{-1}$ ,  $260\text{ cm}^{-1}$ ,  $339\text{ cm}^{-1}$ ,  $676\text{ cm}^{-1}$ , and  $707\text{ cm}^{-1}$  correspond to an  $A_g$  mode and are attributed to internal vibrations of the  $\text{FeO}_6$  octahedra<sup>33–35</sup>. The difference in the scattered light of the samples enhances the  $A_g$  modes, whereas a few other suppressed peaks with lower intensity could be due to  $B_g$  modes<sup>34</sup>, since the vibrational modes are dependent on numerous factors, including crystal orientation, bond strength, particle size, brownmillerite structure, and excitation energy. G and D peaks of rGO were observed in all rGO-CFO composites, and for increased rGO content, the peak intensity increased proportionally.

The oxidation states of constituent elements in CFO and 5rGO-CFO were analyzed using XPS, see Fig. 3a–g. The XPS spectra of Ca 2p of CFO

and 5rGO-CFO, shown in Fig. 3a, d display two peaks arising from the spin-orbit coupling of Ca  $2p_{3/2}$  and Ca  $2p_{1/2}$ <sup>35</sup>. In CFO, these peaks appear at  $\sim 346.2\text{ eV}$  and  $\sim 349.7\text{ eV}$ , respectively, with a binding energy difference of  $\sim 3.5\text{ eV}$ . In the 5rGO-CFO sample, the Ca  $2p_{3/2}$  and Ca  $2p_{1/2}$  peaks appear at  $\sim 347.1\text{ eV}$  and  $\sim 350.7\text{ eV}$ , respectively, with an energy difference of  $\sim 3.6\text{ eV}$ . This implies that in both the CFO and 5rGO-CFO samples, Ca has an oxidation state of  $2+$ . The XPS spectra of Fe 2p for CFO and 5rGO-CFO are shown in Fig. 3b, e. The peaks arising due to spin-orbit coupling, namely Fe  $2p_{3/2}$  and Fe  $2p_{1/2}$ , are further deconvoluted into two peaks, corresponding to octahedral ( $\text{FeO}_6$ ) and tetrahedral ( $\text{FeO}_4$ ) coordination of Fe<sup>20</sup>. In the CFO sample, Fe  $2p_{3/2}$  and Fe  $2p_{1/2}$  peaks corresponding to octahedral ( $\text{FeO}_6$ ) coordination appear at  $710.3\text{ eV}$  and  $723.9\text{ eV}$ , respectively. Tetrahedral ( $\text{FeO}_4$ ) coordination for Fe  $2p_{3/2}$  and Fe  $2p_{1/2}$  peaks appear at  $712.3\text{ eV}$  and  $726.5\text{ eV}$ , respectively. For the 5rGO-CFO sample, the corresponding octahedral peaks appear at  $710.8\text{ eV}$  and  $724.4\text{ eV}$ , respectively, and the tetrahedral peaks appear at  $712.3\text{ eV}$  and  $726.5\text{ eV}$ , respectively. The presence of octahedral and tetrahedral coordination of Fe is clear evidence of ordered oxygen vacancies in brownmillerite  $\text{Ca}_2\text{Fe}_2\text{O}_5$ <sup>20</sup>. The binding energies correspond to Fe 2p, indicating Fe in a  $3+$  oxidation state in both the CFO and 5rGO-CFO samples. The XPS spectra corresponding to O 1s for both the CFO and 5rGO-CFO samples are deconvoluted into two peaks, see Fig. 3c, f, labeled OI and OII. The OI peak corresponding to oxygen in the brownmillerite structure appears at  $529.5\text{ eV}$  and  $530.1\text{ eV}$  for the CFO and 5rGO-CFO samples, respectively<sup>20</sup>. The OII peaks appear at  $531.3\text{ eV}$  and  $532\text{ eV}$ , respectively, for both samples and are attributed to chemisorbed oxygen species<sup>20</sup>. The XPS spectra corresponding to C 1s for the 5rGO-CFO sample are shown in Fig. 3g. The C 1s spectrum is deconvoluted into four peaks located at  $284.6$ ,  $286.1$ ,  $287.3$ , and  $289.4\text{ eV}$ , corresponding to C–C, C–OH, C=O, and O–C=O, respectively. These characteristic peaks are attributed to the presence of rGO<sup>36,37</sup>.

Figure 4a shows the optical absorption spectra of the CFO and 5rGO-CFO composites. After rGO incorporation, the composites exhibit higher optical absorption, which implies that the rGO-CFO samples can absorb visible light better than pure CFO. The optical bandgap for CFO and 5rGO-CFO, 2.1 and 1.9 eV, respectively, was found through the Tauc plot shown in Fig. 4b.

Photoluminescence spectroscopy (PL) has been carried out to examine the charge separation and recombination rate of photo-generated charge carriers in the photocatalysts. Figure 5a shows the PL spectra of the CFO and CFO/rGO nanocomposites. All samples have a very similar broad PL emission peak at 705 nm, with different intensities.

**Fig. 1** | SEM images of samples. **a** CFO, **b** rGO, **c** 5rGO-CFO, and **d** STEM image of 5rGO-CFO.

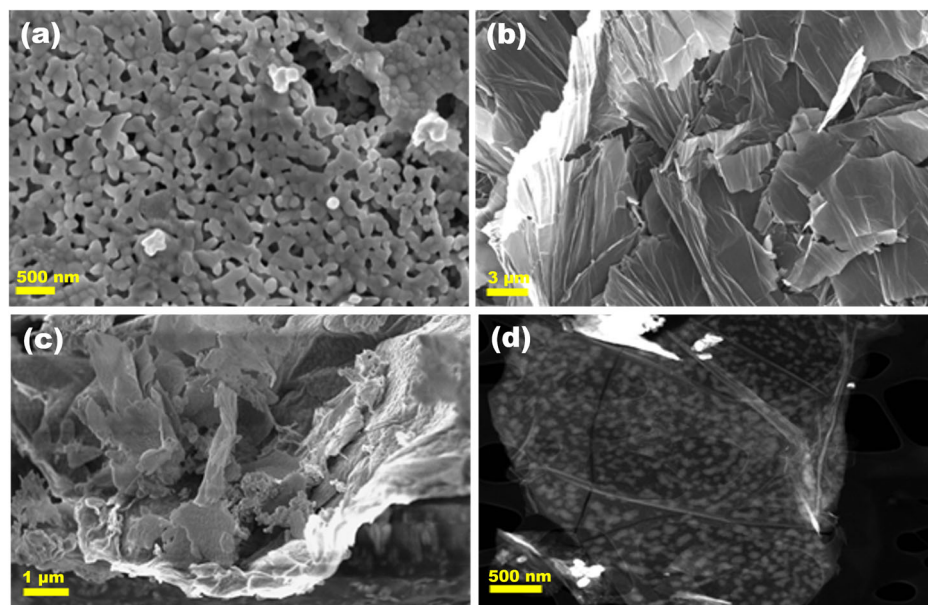


Fig. 2 | XRD pattern and Raman spectra of CFO, GO, rGO, and rGO-CFO nanocomposites. **a** XRD patterns and **b** Raman spectra.

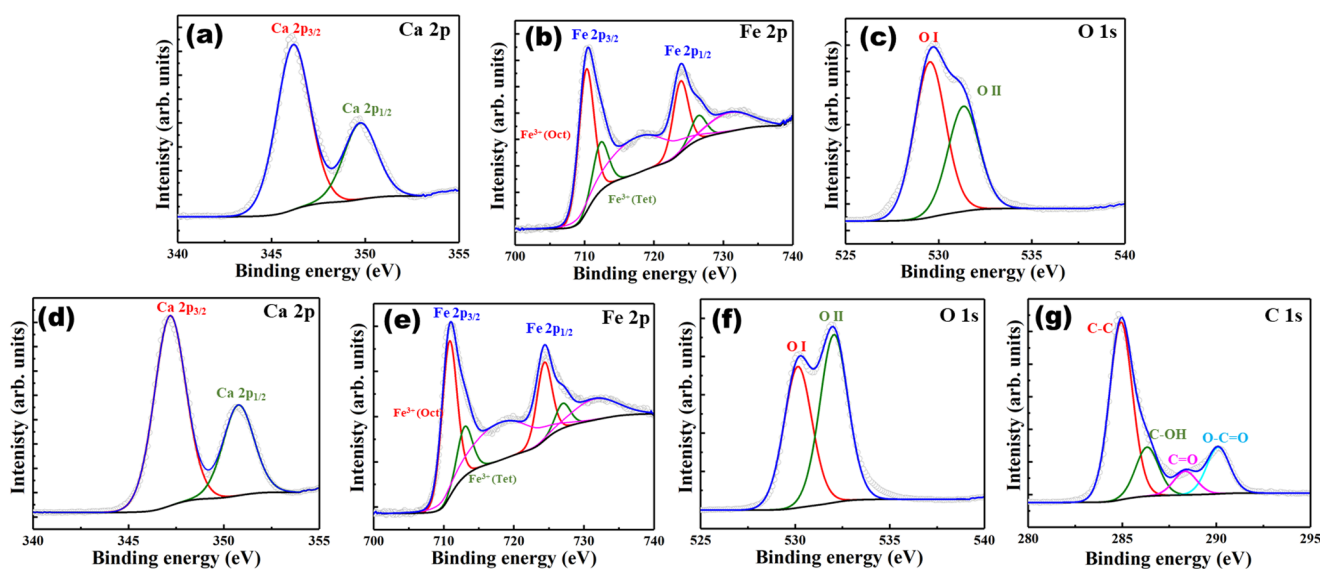
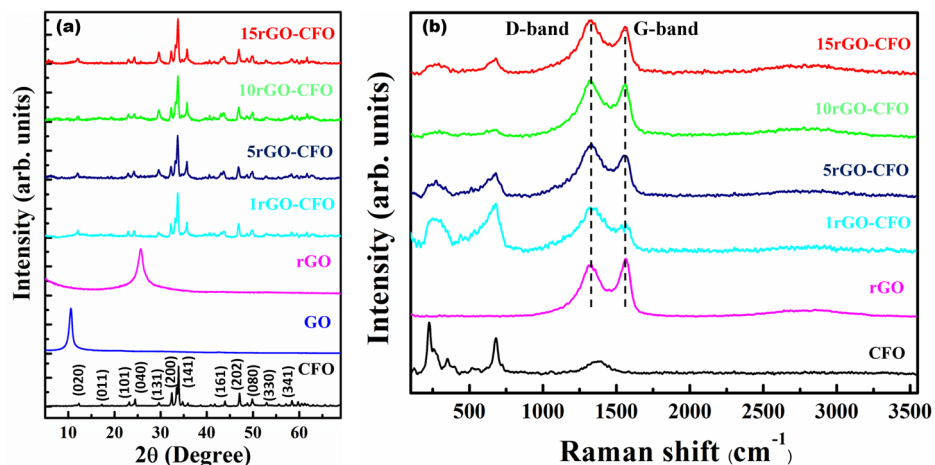
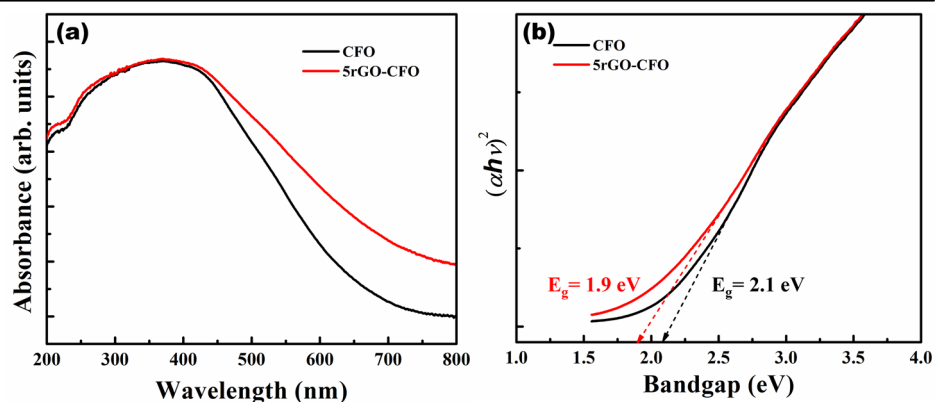


Fig. 3 | X-ray photoelectron spectra (deconvoluted) and corresponding fits for the CFO and 5rGO-CFO samples. **a–c** Ca 2p, Fe 2p, O 1s of CFO and **d–g** Ca 2p, Fe 2p, O 1s, and C 1s of 5rGO-CFO.

Fig. 4 | UV-Visible absorbance and corresponding bandgaps of CFO and 5rGO-CFO. **a** optical absorption spectrum and **b** tauc plots.



In general, high PL intensity means a rapid charge carrier ( $e^-h^+$ ) recombination rate, while a photocatalyst with low PL intensity refers to a low rate of recombination<sup>38,39</sup>. This means that the rGO-CFO composites possess a lower electron-hole recombination rate compared to CFO. In the rGO-CFO composites, rGO acts as a trapping site for

electrons. Consequently, the recombination rate of photoinduced charge carriers is hindered, which is promising for enhancing the photocatalytic activity. The 5rGO-CFO sample has the lowest PL intensity, which implies that 5% of rGO in CFO is the optimal composition for superior charge separation and enhanced photocatalytic activity.



**Fig. 5 | Photoluminescence spectra and Mott-Schottky plots of CFO and rGO-CFO nanocomposites.** **a** PL spectrum of CFO and rGO-CFO nanocomposite and **b** M-S plot of CFO and 5rGO-CFO at 1 kHz frequency.

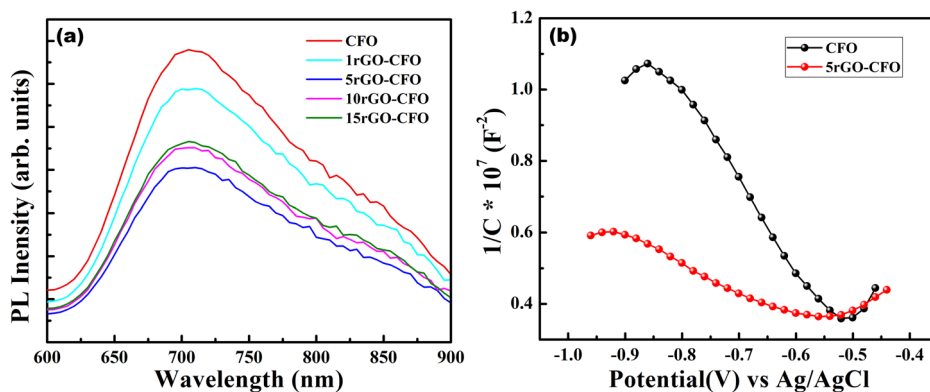
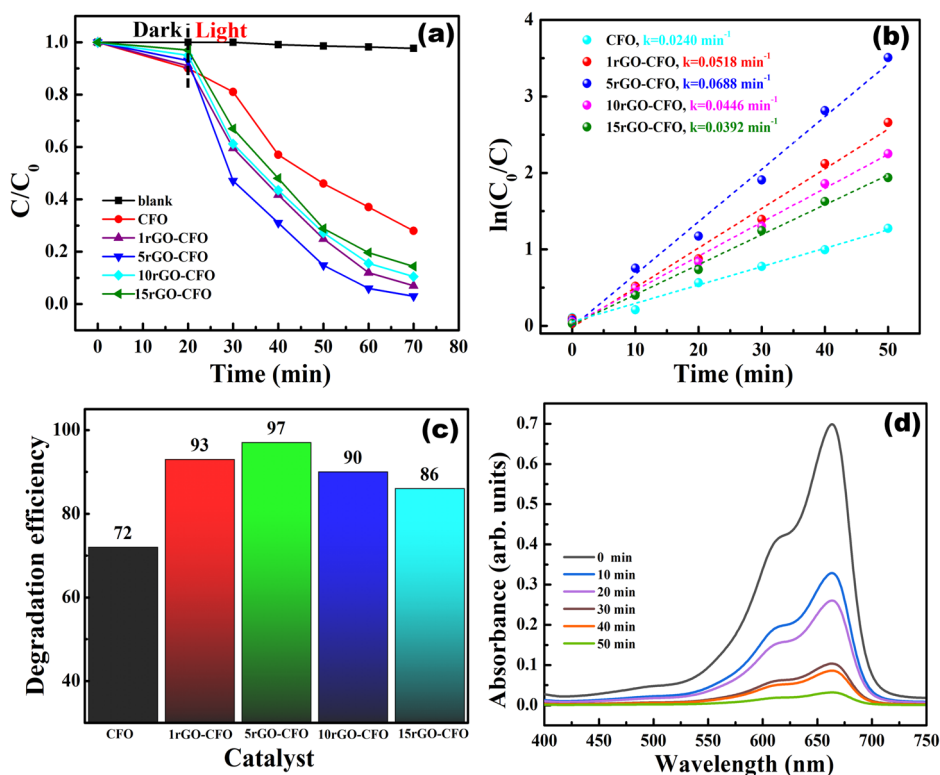


**Fig. 6 | Photodegradation performance of CFO and rGO-CFO nanocomposites for degrading MB.** **a** Photocatalytic degradation ( $C/C_0$ ) of MB using CFO and rGO-CFO composites, **b** first-order reaction kinetics of MB with CFO and rGO-CFO composites, **c** MB degradation efficiency of CFO and rGO-CFO composites, and **d** degradation profile of MB with 5rGO-CFO.



To understand the impact of rGO incorporation on the charge carrier mobility, Mott-Schottky (M-S) tests were performed, shown in Fig. 5b for the CFO and 5rGO-CFO samples. The slope of the M-S curve for 5rGO-CFO is significantly lower than that for the CFO. This means that the charge carrier density of the composite is significantly increased (double) after the incorporation of rGO, which is consistent with previous reports for other metal oxides<sup>40–42</sup>. This is primarily because photogenerated electrons tend to transport through the rGO nanosheets which mitigate charge recombination, thus intensifying available free charge carriers. The incorporation of rGO into the CFO nanocomposite results in higher flat band potential and sufficient band bending (see Fig. 5b), thus providing significant charge separation. Also, the negative slope of the M-S curve for both the CFO and 5rGO-CFO nanocomposites is attributed to a p-type semiconductor.

### Photocatalytic performance

The photocatalytic activity of CFO and rGO-CFO composites was explored by degrading emerging pollutants like MB, BPA, and Tetracycline (TC) under simulated sunlight at standard test conditions (STC) (300 W, Xe-lamp source with 100 mW/cm<sup>2</sup> (1 sun) irradiation). The initial

concentration of each effluent solution (MB, BPA, and TC) was fixed at 10 ppm. All the photocatalysts with a dosage of 0.2 g/l were tested with respect to different wt% of rGO, to find the optimized rGO-CFO composition for efficient photocatalysis. The degradation profile and the reaction kinetics of the CFO and rGO-CFO composites are shown in Fig. 6a–d. The photodegradation efficiency and corresponding rate constants were calculated using Eqs. 1 and 2. Among all the samples, 5rGO-CFO showed the best photocatalytic performance with degradation efficiency at about 97% ( $k = 0.0688 \text{ min}^{-1}$ ), compared to pure CFO (72%,  $0.0240 \text{ min}^{-1}$ ) and the other composites 1rGO-CFO (93%,  $k = 0.0518 \text{ min}^{-1}$ ), 10rGO-CFO (90%,  $k = 0.0446 \text{ min}^{-1}$ ), and 15rGO-CFO (86%,  $k = 0.0392 \text{ min}^{-1}$ ). PL and Mott-Schottky's results showed that the 5rGO-CFO composite has a lower recombination loss compared to the other samples, which implies that more effective charge separation takes place. These photocatalytic degradation results are consistent with PL and Mott-Schottky's results.

To find the optimum 5rGO-CFO catalyst dosage, the MB was degraded with different catalyst concentrations (0.1, 0.2, 0.3, 0.4, and 0.5 g/l), and the  $C/C_0$  and first-order reaction kinetics of the MB degradation is shown in Fig. 7a–c. 0.2 g/l of 5rGO-CFO was found to be the optimum dosage with a

**Fig. 7 | Effect of catalyst loading, and pH on photocatalytic degradation of MB.**

**a** Photocatalytic degradation ( $C/C_0$ ) of MB with various catalyst (5rGO-CFO) concentrations (0.1, 0.2, 0.3, 0.4, and 0.5 g/l), **b** first-order reaction kinetics of MB, and **c** degradation efficiency and rate constant for different 5rGO-CFO concentrations. **d** Effect of different pH values on the MB degradation ( $C/C_0$ ) for the 5rGO-CFO sample.

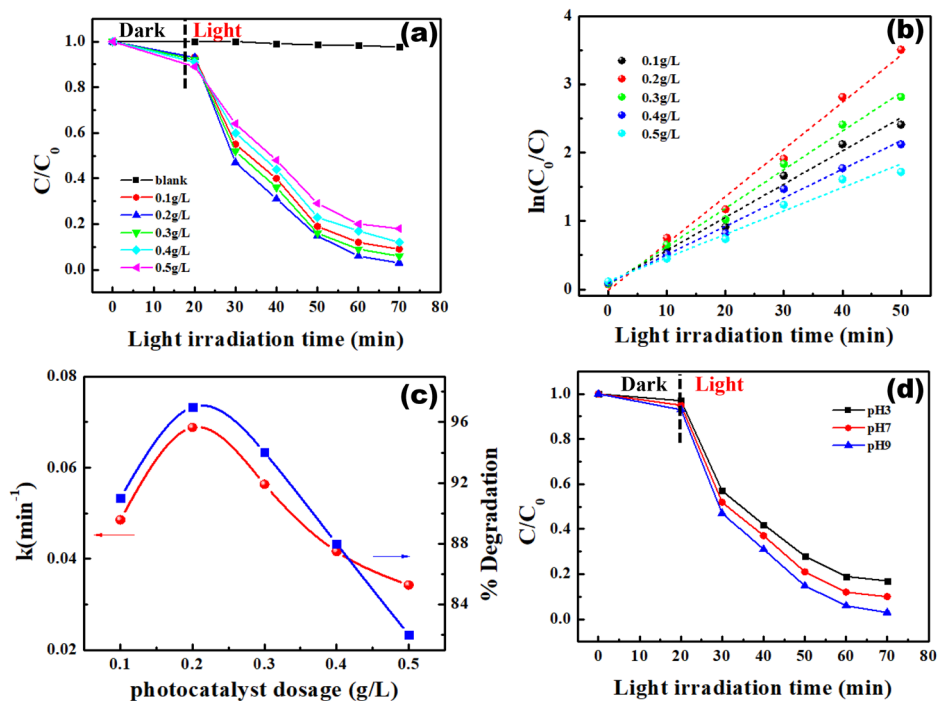
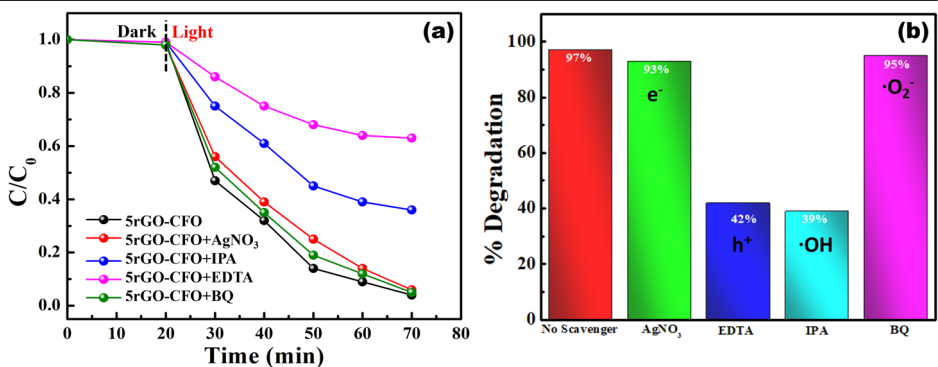


**Fig. 8 | Effect of various scavengers on the degradation of MB for 5rGO-CFO. a**  $C/C_0$  and **b** corresponding degradation efficiency.



degradation efficiency of 97%, see Fig. 7a, whereas other samples showed 91% (0.1 mg/ml), 94% (0.3 mg/ml), 88% (0.4 mg/ml) and 82% (0.5 mg/ml). Without a catalyst, the MB degradation is almost negligible. An overdosage of the catalyst can limit the light penetration into the dye-catalyst suspension and in turn suppress the photocatalytic process. Before the photocatalytic experiments, the suspension with catalyst was kept in the dark for 20 min to achieve adsorption-desorption equilibrium.

$$\text{Degradation efficiency} = \left[ \frac{C_0 - C}{C_0} \right] \times 100 \quad (1)$$

and

$$\ln \frac{C_0}{C} = kt \quad (2)$$

where  $C_0$  and  $C$  are the concentrations of effluent at 0 min and at time interval ' $t$ ' respectively.  $k$  is the degradation rate constant.

The effect of pH on the catalytic reaction was investigated at different pHs; 3, 7, and 9. The pH of the effluent solution was adjusted using 0.05 M HCl and 0.05 M NaOH. The pH of the reaction system plays a major role for the photocatalytic performance because it may prevent the production of

reactive radicals and reduce redox reactions on the surface of the photocatalyst<sup>43–45</sup>. The degradation efficiency of 5rGO-CFO for degradation of MB was analyzed in an acidic (pH 3) and basic (pH 9) reaction system, while the original pH of the MB solution was neutral (pH 7). According to the obtained results depicted in Fig. 7d, when the pH of the solution was tuned from 7 to 9, the photocatalytic degradation efficiency of 5rGO-CFO increased significantly from 92% to 98%. On the other hand, when the pH of the solution was adjusted to 3, the degradation efficiency of 5rGO-CFO dropped considerably from 92% (neutral) to 83%. This shows that the pH value affects the photocatalytic activity considerably. The degradation process occurred favorably in basic pH because of the augmented electrostatic interaction between 5rGO-CFO, MB cations, and readily available hydroxyl ( $\text{OH}^\bullet$ ) radicals, which improves the photocatalytic performance (previously observed in other rGO and metal oxide systems).

**Active species trapping tests.** The photocatalytic mechanism and reactive species involved in the degradation of the MB dye were further studied using active species trapping experiments. For this, 0.5 mM of  $\text{AgNO}_3$ , Ethylenediaminetetraacetic acid (EDTA), Isopropyl alcohol (IPA), and benzoquinone (BQ) were added to the solutions as scavengers to quench electrons ( $e^-$ ), holes ( $h^+$ ), hydroxyl ( $\text{OH}^\bullet$ ) radicals, and superoxide radicals ( $\text{O}_2^{\bullet-}$ ). The effect of the different scavengers on the

**Fig. 9** | Schematic of plausible photocatalytic degradation mechanism of MB for rGO-CFO nanocomposites.

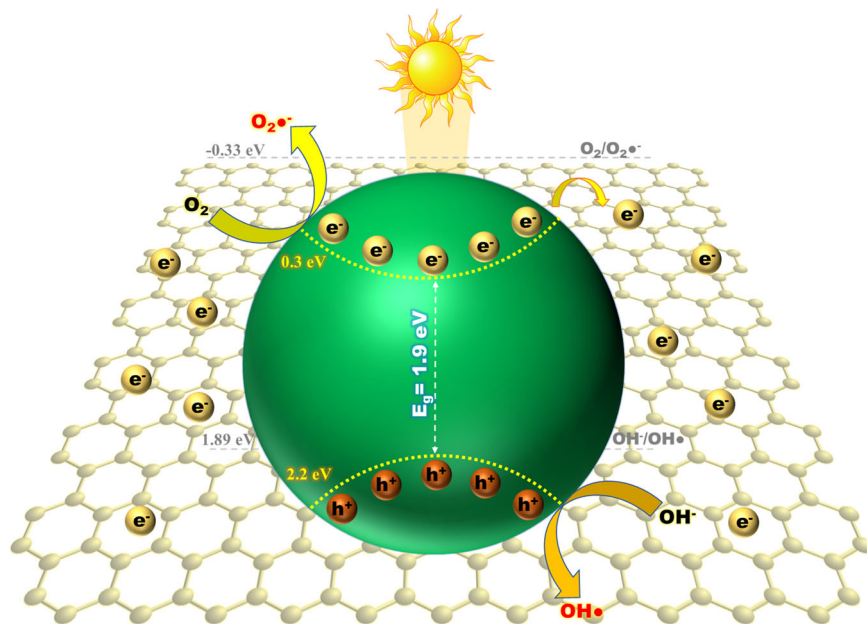
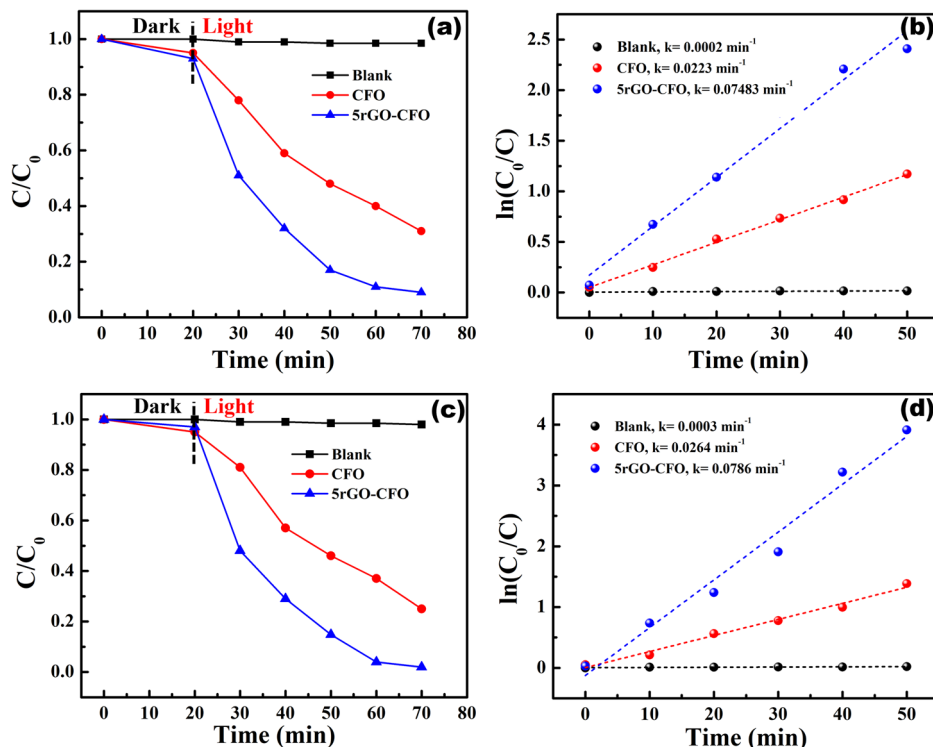


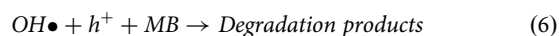
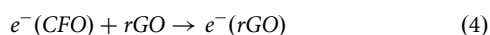
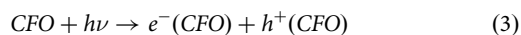
**Fig. 10** | Photocatalytic degradation ( $C/C_0$ ) and first-order reaction kinetics. a, b Bisphenol-A and c, d Tetracycline.



MB degradation efficiency of the 5rGO-CFO composite is illustrated in Fig. 8a, b. The degradation efficiency for 5rGO-CFO was 97% without scavengers. In the presence of EDTA and IPA, the degradation efficiency decreased to 42% and 39%, respectively. This indicates that the OH• radicals and h<sup>+</sup> are the major contributing species for MB degradation. By adding AgNO<sub>3</sub> and BQ to the solution, the MB degradation efficiency dropped to just 93% and 95%, respectively, which indicates that the contribution of e<sup>-</sup> and O<sub>2</sub>•<sup>-</sup> species are insignificant for the photo-degradation of MB. Based on free radical trapping experiments and the valence and conduction band potentials of 5rGO-CFO, the photocatalytic mechanism of the MB degradation could be elucidated. By light

illumination, the photo-generated holes and electrons are generated in the rGO-CFO valence and conduction bands, see Eq. (3), respectively. The photogenerated electrons prefer to transfer from the CFO conduction band to the rGO surface in the presence of rGO nanosheets, which renders it easier to separate the photogenerated electrons and holes in Eq. (4). Besides breaking down the MB molecules, the holes created in the valence band can also generate OH• radicals by interacting with the surface hydroxyl groups in Eq. (5). This can be explained by the OH/OH• redox potential (1.89 eV)<sup>46</sup> being more negative than the rGO-CFO VB hole potential (2.2 eV)<sup>20</sup>. Consequently, repeated reactions with holes and hydroxyl radicals degrade the MB molecules, see Eq. (6). Therefore, it can

be concluded that the highly oxidizing OH• radicals have a higher impact for the decomposition of MB molecules compared to superoxide anion radicals. The reason may be that the conduction band edge potential of CFO (0.09 eV) is more positive than the redox potential of O<sub>2</sub>/O<sub>2</sub><sup>•-</sup> (-0.33 eV)<sup>46</sup>, and thus the formation of superoxide radicals is limited. The MB degradation mechanism obtained by the rGO-CFO nanocomposite is illustrated in Fig. 9.



The degradation intermediates were identified by LC-QTOF-MS. Supplementary fig. 1 shows the LC-MS spectra recorded for solutions before (0 min) and after 25 min and 50 min of photocatalytic reaction. The signal at  $m/z = 284.12$  that was present before the photocatalytic reaction (0 min) was assigned to the pure MB dye molecule<sup>47</sup>. MB molecules were converted into fragments with peaks at  $m/z = 212.14$ , 242.46, 292.05, and 316.54 after 25 min photocatalytic reaction. The peaks  $m/z = 212.14$  and 242.46 were attributed to demethylation through possible N-Methyl ring-breaking reactions. From the active species trapping experiments (above), hydroxyl radicals were acknowledged as the major reactive species to degrade MB molecules. The organics with  $m/z$  of 292.05 and 316.54 were determined by LC-MS, resulting from hydroxylation reactions. An intermediate with  $m/z = 316.54$  could be formed through the addition of two OH• radicals per MB dye molecule, or through the oxidation of methyl (-CH<sub>3</sub>) groups. In addition, the signal at 292.05 is due to the formation of sulfoxide. After 50 min photocatalytic reaction, the LC-MS spectrum shows peaks at lower  $m/z$  values, i.e. 111.27, 122.36, 148.50, and 167.30. This confirms that the dye molecule breaks up into smaller fragments upon degradation and indicates that the discoloration of methylene blue solution (oxidation), catalyzed by rGO-CFO, proceeded via dye degradation (ring rupture).

### Bisphenol-A and tetracycline degradation

The 5rGO-CFO sample was further used to degrade the organic synthetic compound Bisphenol-A (BPA) under simulated sunlight (300 W, Xe-lamp source with 100 mW/cm<sup>2</sup> (1 sun) irradiation). After exposing a BPA-catalyst suspension to light for 50 min, the BPA was degraded about 91% of its initial concentration with a rate constant of  $k = 0.074 \text{ min}^{-1}$ . With CFO, the BPA was degraded about 69% with a rate constant of  $0.022 \text{ min}^{-1}$ . The  $C/C_0$  ratio plots and first-order kinetics are shown in Fig. 10a, b. The 5rGO-CFO composite was also used for degrading the antibiotic Tetracycline (TC), which was degraded by 75% ( $k = 0.026 \text{ min}^{-1}$ ) and 98% ( $0.078 \text{ min}^{-1}$ ) of its initial concentration using CFO and 5rGO-CFO, respectively. The  $C/C_0$  ratio plots and first-order kinetics are shown in Fig. 10c, d.

The LC-MS chromatograms of the time-dependent photocatalytic degradation of TC using 5rGO-CFO composite, measured after 0, 25, and 50 min light irradiation, are shown in Supplementary Fig. 2. Several peaks were observed in the LC-MS spectrum of the untreated TC solution (at 0 min). After 25 min of irradiation, new peaks appear, suggesting that the parent TC molecule has broken down and that intermediate products have been formed. After 50 min of irradiation, with further progress of the photocatalytic reactions, the intensity of the TC peaks has decreased substantially. This indicates that the TC molecule is largely degraded.

Various semiconductor metal-oxides and their composite systems have been widely explored for photocatalytic wastewater treatment, such as TiO<sub>2</sub>, ZnO, SnO<sub>2</sub>, MnO<sub>2</sub>, and WO<sub>3</sub>, for the degradation of various organic effluents<sup>48-52</sup>. A comparison of the photodegradation efficiencies of the rGO-CFO catalyst with other rGO-based composites for MB degradation is

tabulated in Supplementary table 1. The comparison shows the high potential of the materials investigated in the present work. However, the comparison of the photocatalytic performances with state-of-the-art materials is challenging, as photocatalytic degradation experiments are typically conducted under different reaction conditions, like different light sources, catalyst loading, effluent type, effluent concentration, etc. In the present work, we have explored simple and stable brownmillerite oxide and rGO composites for the degradation of Methylene blue, Bisphenol-A, and Tetracycline under simulated sunlight, at standard test conditions, and have assessed their performance. CFO synthesis is simple, scalable, and cost-effective. Processing of single-phase Ca<sub>2</sub>Fe<sub>2</sub>O<sub>5</sub> by solid-state reaction requires relatively high temperatures, often above 1000 °C. In the present work, we adopted a chemical route (which requires a low temperature of 700 °C and a low reaction time of 6 hr), through this we can achieve CFO nanoparticles (~80 nm). This synthesis method requires less energy and time to produce a larger quantity of CFO nanoparticles. rGO-CFO composites are also prepared using a simple thermal reduction method. All the photocatalytic experiments were conducted under simulated sunlight to replicate the natural sunlight-driven photocatalytic water treatment process. The results from sunlight-driven photocatalytic emergent pollutant treatment using low-cost rGO-CFO nanocomposites point towards a greener, comparatively economical, and sustainable treatment method for industrial effluents.

In summary, in this study, a rGO-CFO nanocomposite was prepared by a thermal reduction method. The structural, morphological, and optical properties of the rGO-CFO samples were characterized and studied systematically. Both characteristic bands of the CFO nanoparticles and the rGO nanosheets appeared in the Raman plots, which confirmed the formation of a nanocomposite, further supported by XRD, SEM and STEM results, indicating that spherical CFO nanoparticles were interleaved between rGO nanosheets. The band gap of the rGO-CFO was reduced to 1.9 eV from 2.1 eV (for CFO only). The Mott-Schottky analysis indicated a higher charge carrier density with higher mobility and higher flat band potential after the incorporation of rGO with CFO. The photocatalytic performance of the rGO-CFO composite was optimized for the degradation of effluents under simulated sunlight irradiation. Among the prepared photocatalysts (1, 5, 10, and 15 wt% of rGO), the rGO-CFO composite with 5 wt% rGO had the highest photocatalytic activity. For the optimal catalyst dosage (0.2 g/l), MB was degraded up to 97% in just 50 min. Through scavenger tests, it was further established that holes and OH• radicals are the essential reactive species in the breakdown of MB. By increasing the initial pH of the MB solution, the degradation efficiency of rGO-CFO increased to 98%. 5rGO-CFO was further used to degrade emerging pollutants like Bisphenol-A and Tetracycline, which were degraded over 90% of their initial concentration under light irradiation. Altogether, rGO-CFO nanocomposites show potential as catalyst materials for the photocatalytic degradation of harmful pollutants.

### Data availability

The data sets generated during and/or analyzed during the current study are available from the corresponding author upon reasonable request.

### Code availability

For access to detailed code information, please contact the corresponding author directly.

Received: 26 January 2024; Accepted: 3 May 2024;

Published online: 17 May 2024

### References

- Schlattmann, A. et al. Ecological Sustainability Assessment of Water Distribution for the Maintenance of Ecosystems, their Services and Biodiversity. *Environ. Manag.* **70**, 329–349 (2022).
- Boretti, A. & Rosa, L. Reassessing the projections of the World Water Development Report. *npj Clean. Water* **2**, 15 (2019).



3. Abbass, K. et al. A review of the global climate change impacts, adaptation, and sustainable mitigation measures. *Environ. Sci. Pollut. R.* **29**, 42539–42559 (2022).
4. Lin, L., Yang, H. & Xu, X. Effects of Water Pollution on Human Health and Disease Heterogeneity: A Review. *Front. Environ. Sci.* **10**, 880246 (2022).
5. Okoye, C. O. et al. Toxic Chemicals and Persistent Organic Pollutants Associated with Micro- and Nanoplastics Pollution. *Chem. Eng. J. Adv.* **11**, 100310 (2022).
6. Bashir I. et al. Concerns and Threats of Contamination on Aquatic Ecosystems. In: Bioremediation and Biotechnology: Sustainable Approaches to Pollution Degradation (eds Hakeem K. R., Bhat R. A., Qadri H.). *Springer Int. Pub.* (2020).
7. Patel, M. et al. Pharmaceuticals of Emerging Concern in Aquatic Systems: Chemistry, Occurrence, Effects, and Removal Methods. *Chem. Rev.* **119**, 3510–3673 (2019).
8. Kaur, H. et al. Metal–Organic Framework-Based Materials for Wastewater Treatment: Superior Adsorbent Materials for the Removal of Hazardous Pollutants. *ACS Omega* **8**, 9004–9030 (2023).
9. Al-Nuaim, M. A., Alwasiti, A. A. & Shnain, Z. Y. The photocatalytic process in the treatment of polluted water. *Chem. pap.* **77**, 677–701 (2023).
10. Goyal, N., Amar, A., Gulati, S. & Varma, R. S. Cyclodextrin-Based Nanosponges as an Environmentally Sustainable Solution for Water Treatment: A Review. *ACS Appl. Nano Mater.* **6**, 13766–13791 (2023).
11. Kaczorowska, M. A., Bozejewicz, D. & Witt, K. The Application of Polymer Inclusion Membranes for the Removal of Emerging Contaminants and Synthetic Dyes from Aqueous Solutions—A Mini Review. *Membranes* **13**, 132 (2023).
12. Al-Mamun, M. R., Kader, S., Islam, M. S. & Khan, M. Z. H. Photocatalytic activity improvement and application of UV-TiO<sub>2</sub> photocatalysis in textile wastewater treatment: A review. *J. Environ. Chem. Eng.* **7**, 103248 (2019).
13. Al-Mamun, M. R. et al. Photocatalytic performance assessment of GO and Ag co-synthesized TiO<sub>2</sub> nanocomposite for the removal of methyl orange dye under solar irradiation. *Environ. Tech. Innov.* **22**, 101537 (2021).
14. Amor, C., Marchão, L., Lucas, M. S. & Peres, J. A. Application of Advanced Oxidation Processes for the Treatment of Recalcitrant Agro-Industrial Wastewater: A Review. *Water* **11**, 205 (2019).
15. Ren, G. et al. Recent Advances of Photocatalytic Application in Water Treatment: A Review. *Nanomaterials* **11**, 1804 (2021).
16. Kumari, P. & Kumar, A. Advanced Oxidation Process: A remediation technique for organic and non-biodegradable pollutant. *Results Surf. Interfaces* **11**, 100122 (2023).
17. Ahmed, M. et al. Recent developments in hazardous pollutants removal from wastewater and water reuse within a circular economy. *npj Clean. Water* **5**, 12 (2022).
18. Kader, S., Al-Mamun, M. R., Suhan, M. B. K., Shuchi, S. B. & Islam, M. S. Enhanced photodegradation of methyl orange dye under UV irradiation using MoO<sub>3</sub> and Ag doped TiO<sub>2</sub> photocatalysts. *Environ. Tech. Innov.* **27**, 102476 (2022).
19. Suhan, M. B. K., Shuchi, S. B., Al-Mamun, M. R., Roy, H. & Islam, M. S. Enhanced UV light-driven photocatalytic degradation of methyl orange using MoO<sub>3</sub>/WO<sub>3</sub>-fluorinated TiO<sub>2</sub> nanocomposites. *Environ. Nanotechnol. Monit. Manag.* **19**, 100768 (2023).
20. Vavilapalli, D. S. et al. Nitrogen Incorporated Photoactive Brownmillerite Ca<sub>2</sub>Fe<sub>2</sub>O<sub>5</sub> for Energy and Environmental Applications. *Sci. Rep.* **10**, 2713 (2020).
21. Vavilapalli, D. S. et al. g-C<sub>3</sub>N<sub>4</sub>/Ca<sub>2</sub>Fe<sub>2</sub>O<sub>5</sub> heterostructures for enhanced photocatalytic degradation of organic effluents under sunlight. *Sci. Rep.* **11**, 19639 (2021).
22. Gupta, K., Singh, S. & Ramachandra Rao, M. S. Fast, reversible CO<sub>2</sub> capture in nanostructured Brownmillerite CaFeO<sub>2.5</sub>. *Nano Energy* **11**, 146–153 (2015).
23. Jijil, C. P. et al. Nitrogen Doping in Oxygen-Deficient Ca<sub>2</sub>Fe<sub>2</sub>O<sub>5</sub>: A Strategy for Efficient Oxygen Reduction Oxide Catalysts. *ACS Appl. Mater. Interfaces* **8**, 34387–34395 (2016).
24. Li, Y., Gao, C., Long, R. & Xiong, Y. Photocatalyst design based on two-dimensional materials. *Mater. Today Chem.* **11**, 197–216 (2019).
25. Sharma, D. et al. Visible light activated V<sub>2</sub>O<sub>5</sub>/rGO nanocomposite for enhanced photodegradation of methylene blue dye and photoelectrochemical water splitting. *Inorg. Chem. Commun.* **142**, 109657 (2022).
26. Liu, Y., Zeng, X., Hu, X., Hu, J. & Zhang, X. Two-dimensional nanomaterials for photocatalytic water disinfection: recent progress and future challenges. *J. Chem. Technol. Biot.* **94**, 22–37 (2019).
27. Andreozzi, M. et al. Treatment of saline produced water through photocatalysis using rGO-TiO<sub>2</sub> nanocomposites. *Catal. Today* **315**, 194–204 (2018).
28. Degradation of organic dyes using ZNC/rGO nanocomposite photocatalyst derived from ZIF-8/rGO thermolysis for water treatment. *J. Photochem. Photobiol., A.* **430**, 114001 (2022).
29. Das, D., Das, M., Sil, S., Sahu, P. & Ray, P. P. Effect of Higher Carrier Mobility of the Reduced Graphene Oxide–Zinc Telluride Nanocomposite on Efficient Charge Transfer Facility and the Photodecomposition of Rhodamine B. *ACS Omega* **7**, 26483–26494 (2022).
30. Gupta, K., Singh, S., Ceretti, M., Rao, M. S. R. & Paulus, W. Scaling of extended defects in nano-sized Brownmillerite CaFeO<sub>2.5</sub>. *Phys. Status Solidi (a) Appl. Mater. Sci.* **210**, 1771–1777 (2013).
31. Zaaba, N. I. et al. Synthesis of Graphene Oxide using Modified Hummers Method: Solvent Influence. *Procedia Eng.* **184**, 469–477 (2017).
32. Ghorbani, M., Sheibani, S., Abdizadeh, H. & Golobostanfard, M. R. Modified BiFeO<sub>3</sub>/rGO nanocomposite by controlled synthesis to enhance adsorption and visible-light photocatalytic activity. *J. Mater. Res. Technol.* **22**, 1250–1267 (2023).
33. Dhankhar, S., Bhalerao, G., Ganesamoorthy, S., Baskar, K. & Singh, S. Growth and comparison of single crystals and polycrystalline brownmillerite Ca<sub>2</sub>Fe<sub>2</sub>O<sub>5</sub>. *J. Cryst. Growth* **468**, 311–315 (2017).
34. Piovano, A. et al. Anisotropy in the Raman scattering of a CaFeO<sub>2.5</sub> single crystal and its link with oxygen ordering in Brownmillerite frameworks. *J. Phys. Condens. Matter* **27**, 225403 (2015).
35. Phan, T.-L. et al. Electronic structure and magnetic properties of Al-doped Ca<sub>2</sub>Fe<sub>2</sub>O<sub>5</sub> brownmillerite compounds. *J. Am. Ceram. Soc.* **101**, 2181–2189 (2018).
36. Wei, G., Yu, J., Gu, M. & Tang, T. B Dielectric relaxation and hopping conduction in reduced graphite oxide. *J. Appl. Phys.* **119** (2016).
37. Johra, F. T. & Jung, W.-G. Hydrothermally reduced graphene oxide as a supercapacitor. *Appl. Surf. Sci.* **357**, 1911–1914 (2015).
38. Phanichphant, S., Nakaruk, A., Chansaenpak, K. & Channei, D. Evaluating the photocatalytic efficiency of the BiVO<sub>4</sub>/rGO photocatalyst. *Sci. Rep.* **9**, 16091 (2019).
39. Liqiang, J. et al. Review of photoluminescence performance of nano-sized semiconductor materials and its relationships with photocatalytic activity. *Sol. Energy Mater. Sol. Cells* **90**, 1773–1787 (2006).
40. Dixit, T. K., Sharma, S. & Sinha, A. S. K. Synergistic effect of N-rGO supported Gd doped bismuth ferrite heterojunction on enhanced photocatalytic degradation of rhodamine B. *Mater. Sci. Semicond. Process.* **123**, 105538 (2021).
41. Chen Z. et al. Flat-Band Potential Techniques. In: Photoelectrochemical Water Splitting: Standards, Experimental Methods, and Protocols. Springer New York (2013).
42. Sun, Z. et al. Simultaneously Realizing Rapid Electron Transfer and Mass Transport in Jellyfish-Like Mott–Schottky Nanoreactors for Oxygen Reduction Reaction. *Adv. Funct. Mater.* **30**, 1910482 (2020).
43. Xia, B. et al. Design and synthesis of robust Z-scheme ZnS–SnS<sub>2</sub> n-n heterojunctions for highly efficient degradation of pharmaceutical

- pollutants: Performance, valence/conduction band offset photocatalytic mechanisms and toxicity evaluation. *J. Hazard. Mater.* **392**, 122345 (2020).
44. Bharathkumar, S., Sakar, M., Rohith, V. K. & Balakumar, S. Versatility of electrospinning in the fabrication of fibrous mat and mesh nanostructures of bismuth ferrite (BiFeO<sub>3</sub>) and their magnetic and photocatalytic activities. *Phys. Chem. Chem. Phys.* **17**, 17745–17754 (2015).
45. Liu, Y. et al. Iron Carbon Catalyst Initiated the Generation of Active Free Radicals without Oxidants for Decontamination of Methylene Blue from Waters. *Catalysts* **12**, 388 (2022).
46. Ma, J., Wang, F. & Mostafavi, M. Ultrafast Chemistry of Water Radical Cation, H<sub>2</sub>O<sup>•+</sup>, in Aqueous Solutions. *Molecules* **23**, 244 (2018).
47. Wolski, L. & Ziolek, M. Insight into pathways of methylene blue degradation with H<sub>2</sub>O<sub>2</sub> over mono and bimetallic Nb, Zn oxides. *Appl. Catal. B: Environ.* **224**, 634–647 (2018).
48. Priyadharsan, A. et al. Photocatalytic degradation of organic pollutants and inactivation of pathogens under visible light via SnO<sub>2</sub>/rGO composites. *Chemosphere* **335**, 139102 (2023).
49. Alaizeri, Z. M. et al. Photocatalytic Degradation of Methylene Blue and Anticancer Response of In<sub>2</sub>O<sub>3</sub>/RGO Nanocomposites Prepared by a Microwave-Assisted Hydrothermal Synthesis Process. *Molecules* **28**, 5153 (2023).
50. Ramesh, K., Gnanavel, B. & Shkir, M. Enhanced visible light photocatalytic degradation of bisphenol A (BPA) by reduced graphene oxide (RGO)–metal oxide (TiO<sub>2</sub>, ZnO and WO<sub>3</sub>) based nanocomposites. *Diam. Relat. Mater.* **118**, 108514 (2021).
51. Park, Y., Numan, A., Ponomarev, N., Iqbal, J. & Khalid, M. Enhanced photocatalytic performance of PANI-rGO-MnO<sub>2</sub> ternary composite for degradation of organic contaminants under visible light. *J. Environ. Chem. Eng.* **9**, 106006 (2021).
52. Bekru, A. G. et al. Microwave-Assisted Synthesis of rGO-ZnO/CuO Nanocomposites for Photocatalytic Degradation of Organic Pollutants. *Crystals* **13**, 133 (2023).

## Acknowledgements

J.R. acknowledges funding from the Knut and Alice Wallenberg (KAW) Foundation for a Scholar Grant and Project funding (KAW 2020.0033), and from the Swedish Foundation for Strategic Research (SSF) for a Synergy Program (EM16-0004). The KAW Foundation is also acknowledged for the support of the electron microscopy laboratory at Linköping University. Swedish Research Council (VR) and SSF are acknowledged for access to

ARTEMI, the Swedish National Infrastructure in Advanced Electron Microscopy (2021-00171 and RIF21-0026).

## Author contributions

Conceptualization: D.S.V. Methodology: D.S.V., L.Q. and J.R. Investigation: D.S.V., L.Q. and J.P. Supervision: J.R. All co-authors read and commented on successive drafts of the manuscript.

## Funding

Open access funding provided by Linköping University.

## Competing interests

The authors declare no competing interests.

## Additional information

**Supplementary information** The online version contains supplementary material available at <https://doi.org/10.1038/s41545-024-00334-5>.

**Correspondence** and requests for materials should be addressed to Durga Sankar Vavilapalli or Johanna Rosen.

**Reprints and permissions information** is available at <http://www.nature.com/reprints>

**Publisher's note** Springer Nature remains neutral with regard to jurisdictional claims in published maps and institutional affiliations.

**Open Access** This article is licensed under a Creative Commons Attribution 4.0 International License, which permits use, sharing, adaptation, distribution and reproduction in any medium or format, as long as you give appropriate credit to the original author(s) and the source, provide a link to the Creative Commons licence, and indicate if changes were made. The images or other third party material in this article are included in the article's Creative Commons licence, unless indicated otherwise in a credit line to the material. If material is not included in the article's Creative Commons licence and your intended use is not permitted by statutory regulation or exceeds the permitted use, you will need to obtain permission directly from the copyright holder. To view a copy of this licence, visit <http://creativecommons.org/licenses/by/4.0/>.

© The Author(s) 2024